CCFE
CULHAM CENTRE FOR FUSION ENERGY

UK Atomic Energy Authority

UKAEA-CCFE-PR(22)85

L. Howlett, I. Cziegler, S.J. Freethy, H. Meyer

L-H transition studies on MAST: power threshold and heat flux analysis

L-H transition studies on MAST: power threshold and heat flux analysis

L. Howlett, I. Cziegler, S.J. Freethy, H. Meyer

This is a preprint of a paper submitted for publication in Nuclear Fusion

L-H transition studies on MAST: power threshold and heat flux analysis

Lena Howlett[1,2], István Cziegler[1], Simon Freethy[2], Hendrik Meyer[2], and the MAST team[2]

[1]York Plasma Institute, School of Physics, Engineering and Technology, University of York, York, UK
[2]United Kingdom Atomic Energy Authority, Culham Centre for Fusion Energy, Abingdon, UK

Abstract

Spherical tokamaks are known to differ from conventional tokamaks in a number of physics areas, including in the parameters affecting the L-H transition, but our understanding is limited by a comparative lack of experimental data. A comprehensive study of the density dependence of the H-mode power threshold P_{LH} on the Mega-Amp Spherical Tokamak (MAST) is presented, mapping out the low-density and high-density branches, and describing different types of L-H transitions and intermediate behaviours. Transitions at low densities are characterised by longer preceding 3-4kHz I-phase oscillations or intermittent periods. Commonly used P_{LH} scalings underestimate the experimental values in this data set by at least an order of magnitude, and a fit to the high-density branch gives P_{LH} [MW] $= 11.35 \times \bar{n}_{e20}^{1.19}$, which has a higher density exponent than the scalings. Common understanding of the L-H transition suggests that turbulence is suppressed by sheared $E \times B$ flows in the plasma edge. One mechanism thought to be of importance in the development of a shear in the radial electric field during an L-H transition is the ion heat flux in the edge. Transitions of different densities and neutral beam heating powers were analysed with the interpretative transport code TRANSP, revealing that the total heat flux Q_{tot} possessed a density dependence independent of the net power. The density dependence of the electron heat flux $Q_e \sim 0.62\bar{n}_e$ is stronger than that of the ion heat flux $Q_i \sim 0.15\bar{n}_e$, with Q_i contributing $\sim 12-30\%$ of Q_{tot}. The density dependence is caused by a decrease in beam heating efficiency for both lower densities and for higher injected powers P_{inj}, with the fraction of P_{inj} heating the plasma decreasing from 80% at high densities to 30% at low densities. Low-density or high-P_{inj} discharges appear to have greater fast ion losses, majority orbit and charge-exchange losses, which are seen in Mirnov signals as chirping 50-20kHz modes and broadband MHD at 150-250kHz. The captured beam power estimate by TRANSP does not include the effects of orbit or charge-exchange losses, so appears to be a significant overestimate for low-density plasmas on MAST. If the P_{LH} study is adjusted to account for fast ion losses, in addition to the previously considered shine-through losses, the scatter in H-mode points is reduced and the density exponent is increased to $P_{LH} = 11.27 \times \bar{n}_e^{1.33}$.

1 Introduction

A tokamak plasma can occupy different confinement states, the most well-known being the low confinement L-mode and the high confinement H-mode [1]. During the L-H transition, an edge transport barrier forms just inside the last closed flux surface, and the improved particle and energy confinement leads to a buildup of pressure in the core and a pedestal region with steep gradients in the edge. The higher core pressures generate greater fusion power, making the H-mode a desirable regime for future reactors, and the main operating scenario planned for ITER [2]. Accessing the H-mode requires a minimum amount of heating power, and the dependence of H-mode access on a number of global and local parameters, e.g. wall material [3], plasma current I_p [4], toroidal magnetic field B_T [5], electron density n_e, shaping parameters [6, 7], edge neutral density [8], plasma rotation [9, 10], has been studied on numerous tokamaks under different conditions. The minimum net power P_{net} required for H-mode access is known as the threshold power P_{LH} and has many parameter dependencies, with most not yet quantified. P_{LH} is a fairly crude measure to describe H-mode access conditions and does not readily reveal information on

the physics of the L-H transition, but as a comprehensive model to replace it has not yet been developed, P_{LH} is currently still a necessary measure and regularly in use. Regardless of the values or items chosen for the other parameters, the line-averaged density dependence of P_{LH} appears to follow a similar trend for most devices (e.g. JET [4], C-Mod [5], ASDEX Upgrade [11], HL-2A [12]), a non-monotonic relationship with a low- and a high-density branch. For densities above the density of minimum P_{LH}, known as $n_{e,min}$, P_{LH} increases with increasing density, i.e. H-mode access requires higher powers. For densities below $n_{e,min}$, there appears to be a steep inverse relationship between density and P_{LH}, finally suggesting something like a low-density limit for H-mode access.

Much work had been done since the discovery of the H-mode to obtain a physical model for the L-H transition, and several connected phenomena before and during the transition are thought to play an important role. It is universally accepted that the improved confinement in H-mode is due to a reduction in anomalous cross-field transport, i.e. turbulence. Turbulence is suppressed by interaction with sheared $E \times B$ flows in the plasma edge, just inside the separatrix. The sheared mean flows form a predator-prey relationship with the turbulence, until a critical kinetic energy transfer from turbulence to the mean flows suppresses the turbulence and the plasma transitions to a new confinement state, H-mode [13]. The shear flow can be generated through neoclassical effects, or, in case of zonal flows, created through a self-generation by turbulent stresses. One observation common throughout different devices is the existence of a well in the radial electric field E_r profile which grows more negative at the transition [14, 15]. It is thought that the strong E_r shear induced by the ∇E_r in the edge could produce the necessary sheared $E \times B$ flow for turbulence suppression. Neoclassical theory suggests that the gradient of the ion temperature plays a significant role in the E_r profile, and studies on several devices have found a link between the ion heat flux q_i at the edge and the L-H transition [16, 17], which is also consistent with the zonal flow picture of L-H transition dynamics [18].

While the physical basis of the transition is now better understood, it is still not currently possible to predict P_{LH} for a new tokamak or scenario using these models, and many parameter dependencies shown in experimental evidence are lacking in a theoretical explanation for their effects. From the large database of experiments performed on H-mode access, an empirical scaling law for the high-density branch of P_{LH} capturing some of the dependencies has been developed by Martin et al. in 2008 [19]. This scaling law is an approximation only valid in a limited range of conditions, and crucially does not accurately describe the P_{LH} behaviour for low aspect ratio or spherical tokamaks (ST) such as MAST. While most devices are based on the conventional tokamak concept with aspect ratio $A > 2$, spherical tokamaks represent an alternative design with $A \sim 1.1-1.8$ and a more compact vessel shape, allowing operation at high plasma beta $\beta = 2\mu_0 p/B^2$ without becoming ballooning unstable, so that lower magnetic fields B are required to reach the same plasma pressure p as a conventional device. STs are a potentially promising concept for fusion power plants, and the first such prototype being designed in the UK, STEP, is based on an ST concept. Due to the strong shaping and other defining features of STs, some aspects of tokamak physics behave differently for STs compared with conventional tokamaks. This includes the L-H transition, as demonstrated by the fact that the P_{LH} scaling laws, based on mostly conventional tokamak data, have been shown to significantly underestimate P_{LH} for the STs NSTX and MAST [19]. Scaling laws capture a limited number of parameter dependencies, and some of the parameters which are not included are thought to play a more prominent role in STs. The comparatively small amount of ST data and the lack of dedicated L-H studies on them has made determining the cause of this discrepancy challenging. While previous STs like NSTX and MAST have been fairly similar devices, there is much more scope in variation for STs, and knowing under what conditions STs have a higher P_{LH} as well as whether they follow the same parameter dependencies as have been found on conventional tokamaks is crucial for the development of new STs like STEP. A reasonable estimate of P_{LH} is necessary to be able to incorporate the required auxiliary heating power into the design.

This paper is structured as follows: The experimental conditions of the data used in this analysis are described in Section 2, while Section 3 introduces the method for calculating P_{net}. Section 4 introduces and describes the plasma behaviour categorisations used in this paper. The results of the power threshold analysis are presented in Section 5, along with comparisons to scaling laws and a fit to the data. Section 6 presents an ion and electron heat flux analysis as a comparison of one potential L-H transition mechanism with results from other devices. A summary and conclusions of the paper are outlined in Section 7.

2 Experimental Setup

MAST [20] is a medium-sized spherical tokamak with an aspect ratio of $R/a = 0.85\text{m}/0.65\text{m} \sim 1.3$, graphite walls and auxiliary heating provided by neutral beam injection (NBI). The data in this paper

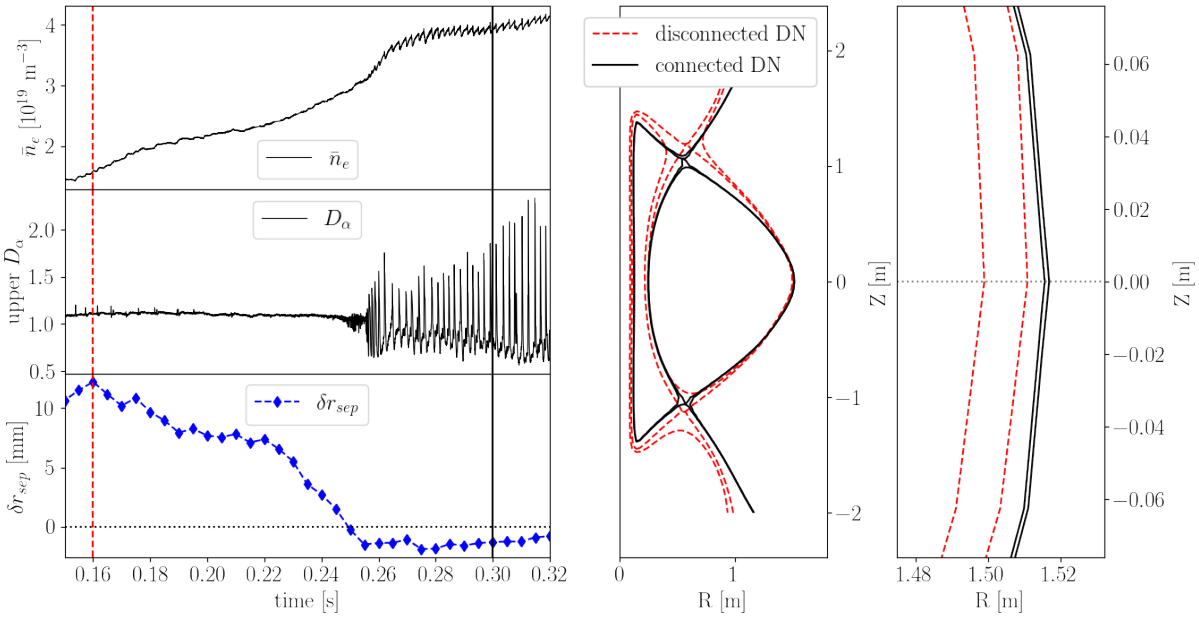

Figure 1: Line averaged density $\bar{n}_e$, upper D_α and δr_{sep} traces for a shot which transitioned from L- to H-mode shortly after the configuration was changed from a disconnected double null (DDN) to a connected double null (CDN). The separatrices for two time points, one during DDN phase (red dashed) and one during CDN (black) are shown in the middle. The δr_{sep} variable corresponds to the midplane distance between the two separatrices associated with each X-point, and the larger value for DDN can be seen in the zoomed in plot on the right.

is taken from L-H transition experiments with shot numbers between 27035 and 28330. The shots included in the analysis have plasma currents of $I_p = 740 \pm 20$kA, are stabilised in connected double null configurations with $\delta r_{sep} = 0.0 \pm 1.5$mm, have elongations of $\kappa = 1.78 \pm 0.05$, and upper and lower triangularities of $\delta_l = 0.48 \pm 0.01$ and $\delta_u = 0.47 \pm 0.01$. For the main purpose of the experiment, the NBI heating power and the plasma density were varied, while keeping the rest of the plasma as consistent from shot to shot as possible. Not counting further density increases during H-mode, the density was varied between 0.15 and 0.63 n_G, where the Greenwald density $n_G = I_p/(\pi a^2)$ (units of 10^{20} m^{-3}, MA and m) describes an operational limit for the density in MCF devices [21]. The density peaking generally decreases with increasing line averaged density from 1.8 to about 1.2 in the presence of a partial or full transport barrier and is 1.3 ± 0.1 in L-mode.

For plasmas in a double null configuration, i.e. both upper and lower divertor carrying a significant amount of the exhaust, the timing of the L-H transition can be controlled through shifting the plasma somewhat towards the unfavourable "upper" divertor initially, before balancing the power loading at a later chosen time [22]. This is possible as the upper single null configuration, which would be the extreme version of this bias, is an H-mode unfavourable configuration, where the ion grad-B drift points away from the main X-point and the required threshold power is significantly higher than for the opposite case [23]. This H-mode control technique was used in this experiment to allow for precise timing of diagnostics for study of the L-H transition. The technique can be observed in the trace of the radial distance between the two separatrices at the midplane δr_{sep}, which is reduced to ~ 0mm as the plasma is balanced to connected double null. Figure 1 shows the δr_{sep} trace and associated equilibria of a shot which transitioned to H-mode shortly after reaching the connected double null configuration.

3 Net power calculation

Determining P_{LH} requires the calculation of the net power P_{net}, which can be defined as either the loss power P_{loss} or the power crossing the separatrix P_{sep}. Both versions include the ohmic heating P_{ohm}, the auxiliary heating, which for MAST is the NBI heating power P_{nbi} absorbed by the plasma, as well as the rate of change of stored energy W in the plasma, i.e. dW/dt. P_{sep} additionally includes the power radiated from the core P_{rad}, with a majority contribution from Bremsstrahlung losses. Most

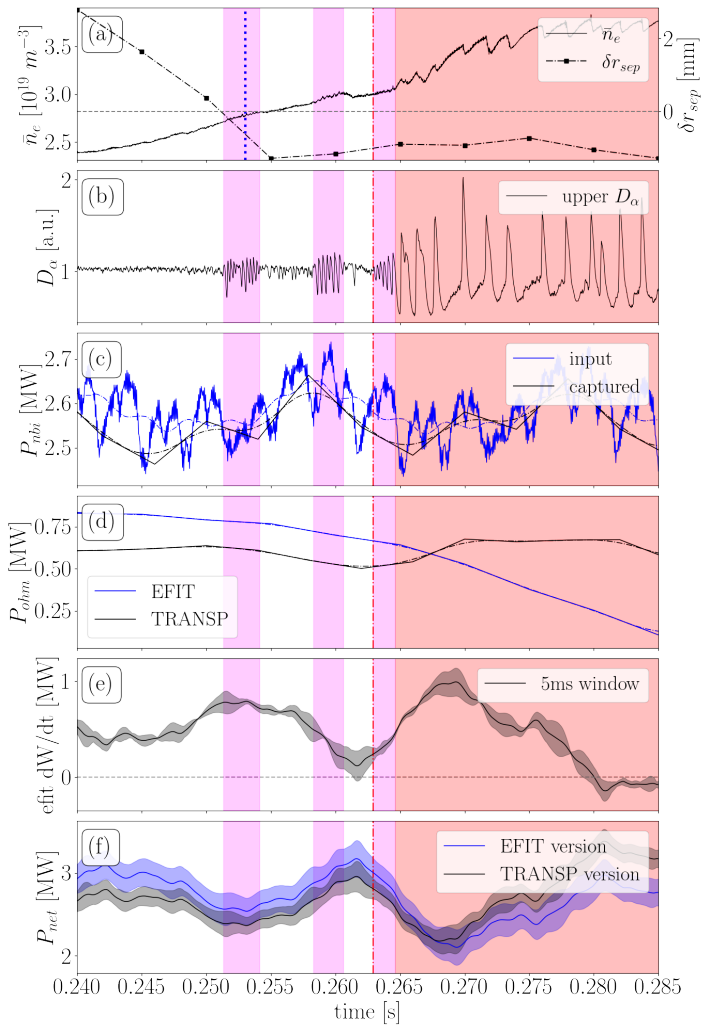

Figure 2: For an example H-mode shot, traces of (a) line averaged density and δr_{sep}, (b) deuterium Balmer α (D_α), (c) injected and captured P_{nbi}, (d) two estimates for P_{ohm}, (e) the rate of change of stored energy with an uncertainty range based on smoothing window size, (f) P_{net} results and uncertainties for the EFIT and TRANSP versions. Note the rise in dW/dt starting with the pre-H I-phase. The blue dotted line in (a) marks the start of the constant δr_{sep} period, which for this shot occurred 10ms before the transition (red dashed line).

power threshold studies as well the scalings [19] take $P_{net} = P_{loss}$. In this paper, both versions were calculated and the results presented, though for MAST P_{rad} was generally found not to be of qualitative significance, and P_{net} is used to refer to P_{loss}. The net power calculation is thus summarised as:

$$P_{loss} = P_{ohm} + P_{nbi} - \frac{dW}{dt} \left(= P_{net}\right), \tag{1}$$

$$P_{sep} = P_{loss} - P_{rad}. \tag{2}$$

For the P_{net} calculations, both the equilibrium code EFIT [24] and the transport code TRANSP [25] were utilised. For the NBI power, there can be significant discrepancies between the injected power and the power absorbed by the plasma, especially in low-density scenarios, where reduced attenuation of the beam by the plasma can lead to shine-through losses [26], so an estimate of the captured beam power calculated by TRANSP is used. The beam power modulation provides an estimate for the uncertainty on P_{nbi}. Since the dW/dt term involves the calculation of a gradient of a time series, a high time resolution in the stored energy is preferred, and dedicated EFIT runs with a time resolution of 0.6ms were utilised. Since W is a discrete signal with limited time resolution and noisy data, the time series were smoothed before dW/dt was calculated. The size of the smoothing window can be varied to optimise noise filtering and signal feature preservation, and a smoothing window size of 5ms was selected. The effect of smoothing window choice was estimated by including the range of dW/dt results for window sizes between 2ms and 8ms as a source of uncertainty on dW/dt. Where it is included, the radiated power is estimated from data of the bolometry diagnostic. The ohmic power can be approximated by the product of the plasma current and the loop voltage, and the final value used for P_{net} can be calculated either with TRANSP or with EFIT. While the TRANSP result is preferred, approximately 10% of the shots in this data set did not achieve successful TRANSP runs, so two methods for P_{net} were compared, the TRANSP method with P_{ohm} and captured P_{nbi} from TRANSP, and the EFIT method with injected P_{nbi} and P_{ohm} as calculated by EFIT. Due to the aforementioned shine-through phenomenon, the second method overestimates P_{net} for low-density shots, but as the difference between the two P_{ohm} versions (see Figure 2) is negligible compared with P_{net}, the qualitative results of this study described in later sections are similar for the two methods.

4 Plasma behaviour categorisation

For L-H transition studies, the identification of the plasma's confinement state as well as times of transitions between states are necessary, but in practice this can be difficult to identify clearly. Plasmas close the H-mode boundary or of low density can exhibit more complex behaviours that are not immediately categorised as either an L-mode or an H-mode, making the identification of L-H transition times challenging. Based on their signatures in relevant traces, a number of distinct though potentially related behaviour categories were identified. These intermediate categories as well as the sub-classification of H-modes are introduced and described in the following section, after a general overview of how L-H transitions are usually identified.

The behaviour categories and the inter-category transition times can be identified as a first step from visual inspection of the D_α and line averaged density $\bar{n}_e$ traces. The transition from L- to H-mode is visible as a drop in D_α signal coinciding with a steep rise in $\bar{n}_e$, corresponding to the change in confinement quality leading to an accumulation of density and a reduced level of interaction with neutrals, which is the main source of D_α emission. H-modes are also characterised by a reduction in fluctuations visible in turbulence diagnostics and the formation of a density and temperature pedestal in the profiles measured by the Thomson scattering diagnostic. H-modes are usually unstable due to the steep edge gradients, accumulate large amounts of fuel and impurity particles, and will often expel these accumulations in edge localised modes (ELMs) [27].

The intermediate categories are seen both during transition from L- to H-mode and at net powers close to P_{LH}. Discussions around some of these phenomena with respect to their identities and their relation to each other and to L- and H-mode are ongoing, with no consensus reached yet between different devices and research groups, so a standardised nomenclature is not available. For this paper, the chosen categories have been named to be internally consistent with some input taken from previous work.

- **I-phases**: distinctive regular 3-4kHz oscillations (sine-like in upper D_α and miniature ELM-like in midplane D_α). Found at $\bar{n}_e \sim 1.6 - 3.2 \times 10^{19}$ m^{-3}. Examples shown in Figure 3h-i.
- **pre-H I-phases**: I-phase preceding an H-mode. In some cases, the I-phase oscillations will evolve by skipping peaks, decreasing in frequency and growing in amplitude until the H-mode period

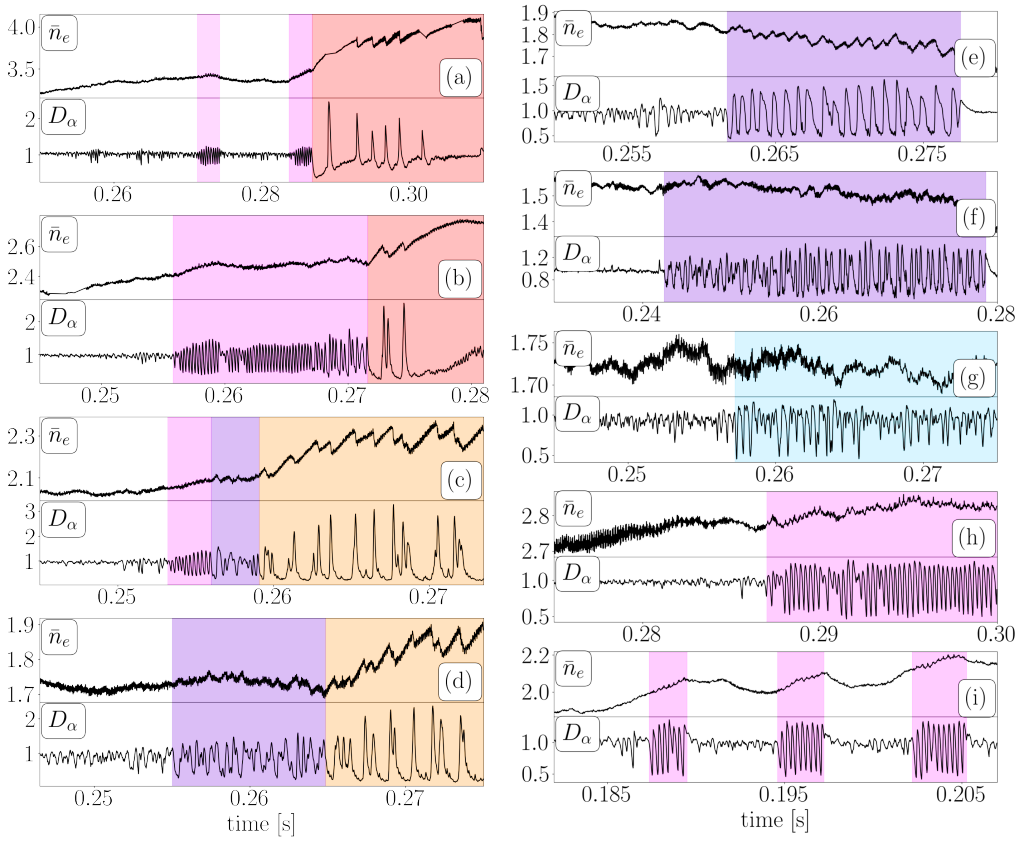

Figure 3: Example $\bar{n}_e$ and D_α traces for behaviour categories: (a) ELMy H-mode with intermittent preceding I-phases, (b) H-mode with long continuous preceding I-phase which displays the peak-skipping evolution towards the end, (c) and (d) dithery H-modes, (e) and (f) show dithery periods that did not reach H-mode confinement levels, (g) shows intermittent dithering, while (h) shows a long continuous I-phase and (g) intermittent short I-phases. I-phases are coloured in fuchsia, dithery periods in purple, intermittent dithering in light blue, dithery H-modes in orange and conventional H-modes in red.

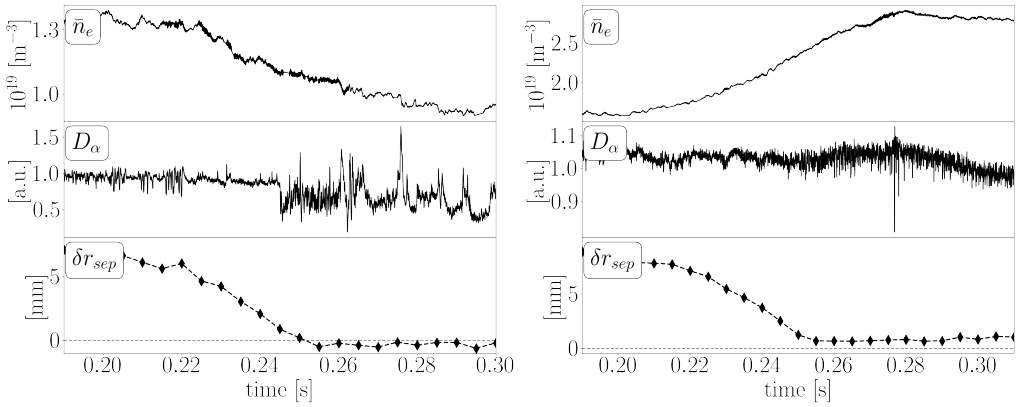

Figure 4: Examples of a low-density (left) and a high-density (right) L-mode, with $\bar{n}_e$, D_α and δr_{sep} traces. The low-density case shows the beginning of an active period as δr_{sep} is lowered to connected double null, whereas the high-density case is fairly quiet (note also the magnitude of fluctuations in D_α).

begins, as seen in Figure 3b. The pre-H I-phase length is usually 2-3ms ($\sim 0.1\tau_E$), but can be up to 10-30ms ($\sim \tau_E$) for $\bar{n}_e \sim 2.0 - 2.5 \times 10^{19}$ m^{-3}. Examples shown in Figure 3a-c.

- **H-modes**: most H-modes in this study are type-III ELMy, with ELM frequency $f_{ELM} \sim 500 - 600$Hz, consistent with expected values for the studied densities on MAST [28]. The transition either occurs directly from L-mode or through one or more pre-H I-phase periods. Transitions occurred at $\bar{n}_e \sim 2.0 - 3.3 \times 10^{19}$ m^{-3}. Examples shown in Figure 3a-b.
- **dithery H-modes**: low-density H-modes with irregular ELMs, including double- or triple-ELMs. Each ELM filament expels a larger fraction of the density and the H-modes are more difficult to sustain. Found at $\bar{n}_e \sim 1.7 - 2.2 \times 10^{19}$ m^{-3}. Examples are shown in Figure 3c-d.
- **dithery periods**: clearly defined periods of irregular fluctuations in D_α but confinement below H-mode levels. Occur at low plasma density, $\bar{n}_e \sim 1.2 - 1.8 \times 10^{19}$ m^{-3}. Examples shown in Figure 3d-f.
- **intermittent dithering**: noisy or L-mode-like dithery periods without clearly defined start and end points. Occur at similar densities to **dithery periods** but lower powers. Example shown in Figure 3g.
- **L-mode**: default state of the plasma, assigned based on exclusion of other categories. Low-density L-modes appear "choppy" while high-density L-modes appear "quiet" (see Figure 4).

It is likely that the dithery periods and I-phases are not entirely distinct phenomena but rather aspects of the same mechanism, such as limit-cycle-oscillations (LCOs). The label "dithery" is used here to highlight the irregular nature of the fluctuations in those categories, especially contrasted with the strong regularity of I-phase fluctuations.

From visual inspection of the D_α signals, the differences between the behaviour categories can clearly be qualitatively defined, as can be seen in Figure 3. In order to solidify the categorisations further, quantitative differences especially between the intermediate categories (dithery and I-phases) were investigated. The upper and midplane D_α signals were analysed for fluctuation frequencies, skewness and kurtosis of each time period associated with an I-phase, a pre-H I-phase, an ELMy H-mode, a dithery H-mode, a dithery period or an intermittent dithering period. The signatures of the different categories are most clearly visible in the upper D_α signal, so the analysis was concentrated on those traces.

The clearest separation of categories was found in the frequency-skewness space, as can be seen in Figure 5. I-phases and pre-H I-phases are clustered around their characteristic fluctuation frequency of 3-4kHz, and ELMy H-modes reveal an ELM frequency of 500-600Hz, which is consistent with the expected f_{ELM} at the studied densities on MAST [28]. I-phases have a skewness close to zero, which corresponds to their sine-like quasi-symmetrical shape in the upper D_α time signals. ELMy H-modes have strong positive skewness, consistent with the expected ELM behaviour, however, H-modes with higher f_{ELM} have lower values of skewness. Dithery periods are found spread out at frequencies between ELMy H-modes and I-phases, mainly 1.5-2.5kHz. The irregular nature of their fluctuations means that a single frequency is not quite as appropriate a characterisation in their case. The different types of dithery period are separated in their values of skewness, with those of higher confinement quality such as dithery H-modes having positive skewness and the intermittent dithering periods which are almost L-mode-like more negatively skewed.

4.1 Note on transition time selection

Another feature of H-modes is the rise in stored energy W due to the improved confinement. In those H-mode shots with a pre-H I-phase period, W begins increasing at the start of this period, as the average confinement increases due to the intermittent periods of improved confinement. The pre-H I-phase appears clearly linked to the subsequent H-mode periods, as also shown in some shots which had a somewhat continuous transition from I-phase into H-mode through a period in which I-phase peaks in D_α are skipped in regular intervals, reducing the frequency and increasing the amplitude to an intermediate stage between those of the I-phases and ELMs (see Figure 3b). This picture is consistent with studies of the I-phases or LCOs on ASDEX Upgrade, which have shown that the I-phase contains many H-mode characteristics and proposed that the L- to I-phase transition is more relevant to L-H studies than the I-phase- to H-mode transition [29]. For the following results, the transition time is taken as the L-mode→I-phase transition for H-modes with a preceding I-phase, and the L-mode→H-mode transition

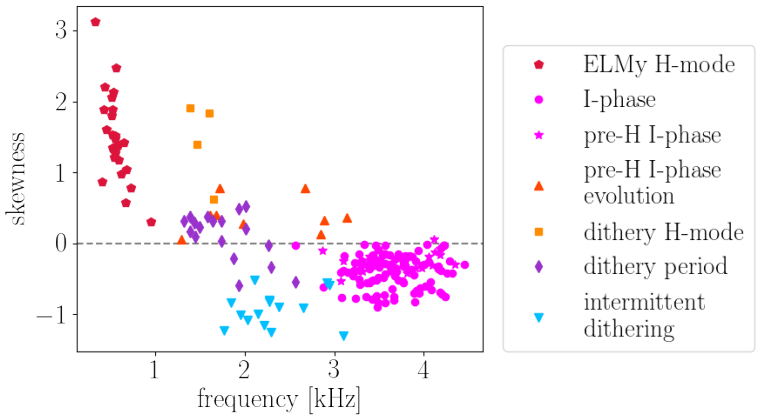

Figure 5: The peak frequency and skewness for upper D_α timeslices of the different categories. ELMy H-modes and I-phases are well separated from the dithery categories in frequency, and the three dithery categories are distinguishable in skewness. The pre-H I-phase evolution points (the peak skipping behaviour seen in Figure 3b) are spread out but shifted in frequency and skewness from the I-phase values towards the H-mode values.

for those without an I-phase. As an aside, Figure 7 shows the effect on $P_{net}(\bar{n}_e)$ of taking the second transition (I-phase→H-mode) instead for H-modes with an I-phase. Due to the increase in both density and stored energy during the I-phase, the points are shifted to a different parameter space, and in the density range for most H-modes the new points overlap with the L-mode parameter space. For all other results, the L-mode→I-phase transition is chosen.

5 Density dependence of P_{LH} on MAST

For each transition or equivalent L-mode point, the net power P_{net} is plotted against the line-averaged density $\bar{n}_e$, with the main results of this study shown in Figures 6 and 8. As mentioned in Section 3, P_{net} can be calculated using one of two definitions and one of two methods. All four options were considered, and as can be seen in Figure 8, no significant qualitative difference was found between the results of the TRANSP method and the EFIT method, aside from a larger spread in P_{net} values at low densities for the EFIT case which is to be expected from using the injected power instead of the captured power for P_{nbi}. The effect of P_{rad} was also studied, but aside from the expected general reduction of the net power values, the results were not affected, as seen in Figure 6.

The boundary separating the H-mode-accessible and -inaccessible regions reveals a similar non-monotonic U-shaped density dependence as seen on other devices (e.g. JET [4], C-Mod [5], ASDEX Upgrade [11], HL-2A [12]). H-modes are sparse in the density range below $2.5 \times 10^{19} m^{-3}$, but the minimum of the P_{LH} curve, $n_{e,min}$ appears to lie in the region of $2 - 2.5 \times 10^{19} m^{-3}$ with a minimum P_{LH} of around 2MW. H-modes above $2.5 \times 10^{19} m^{-3}$ are ELMy, with no or short pre-H I-phases, while H-modes below this density have longer pre-H I-phases or are dithery. I-phases with no subsequent H-mode are found at the P_{LH} boundary in a wide range for $\bar{n}_e > 1.6 \times 10^{19} m^{-3}$. Dithery periods are located on the low-density branch, in a narrower density range of $1.2 \times 10^{19} m^{-3} < \bar{n}_e < 2 \times 10^{19} m^{-3}$ but a wider P_{net} range, reflecting the steep increase in the low-density branch. Due to the lack of low-density H-modes, the dithery periods were actually required to define the P_{LH} boundary in the low-density branch. Intermittent dithering is found at lower powers than the clear dithery periods, presumably further away from P_{LH}. L-modes are ubiquitous both at very low densities and at higher densities and lower powers (see Figure 4 for the different appearance in the two cases), but it is harder to achieve lasting L-modes around $n_{e,min}$, especially without considering purely ohmically heated shots.

5.1 Comparison with scaling laws

Several empirical scaling laws for P_{LH} have been derived from large multi-machine databases, including the widely used ITER scaling from Martin et al. [19]

$$P_{LH}^{M} = 0.0488 \bar{n}_{e20}^{0.717} B_T^{0.803} S^{0.941} \tag{3}$$

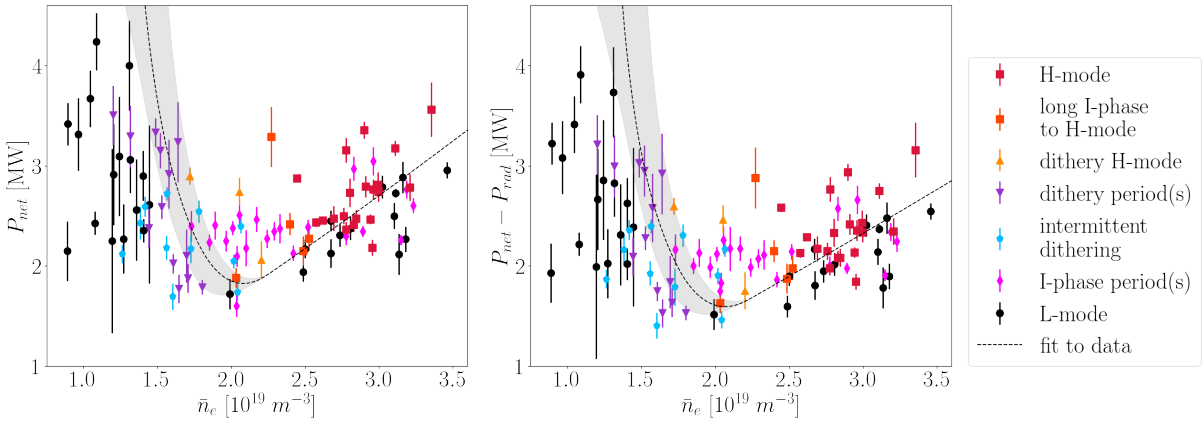

Figure 6: P_{net} vs $\bar{n}_e$ results for the TRANSP method, without P_{rad} (left) and with P_{rad} (right).

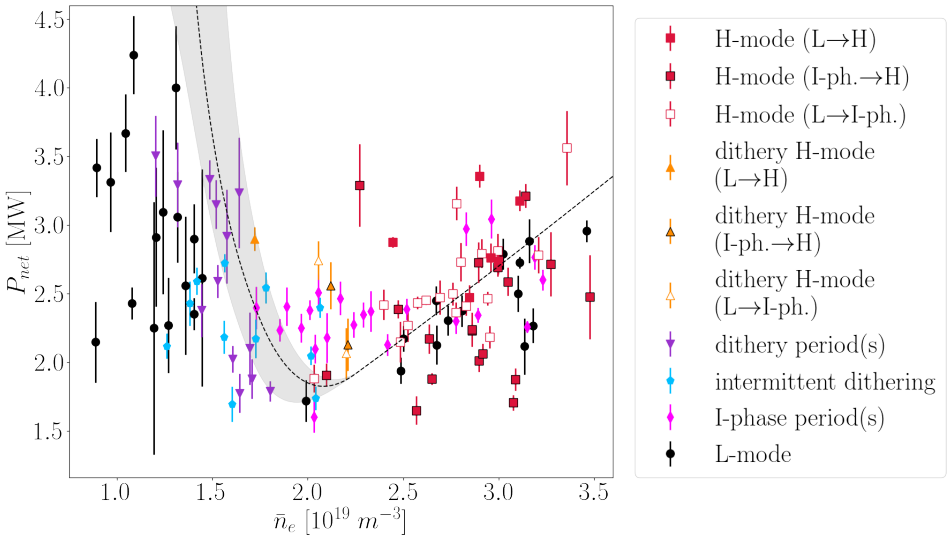

Figure 7: P_{net} vs $\bar{n}_e$ results for the TRANSP method, showing the impact of the pre-H I-phase in the transition time selection for H-modes. For H-modes and dithery H-modes, solid symbols are transitions which occurred without an I-phase, open-faced symbols are the transitions from L-mode to pre-H I-phase (which are used as the transition times for all other figures, see e.g. Figures 6 and 8), and symbols with black borders are for transitions from I-phase to H-mode. Due to the increase in density and stored energy during the I-phase, I-phase→H-mode transitions are located further into the L-mode parameter space.

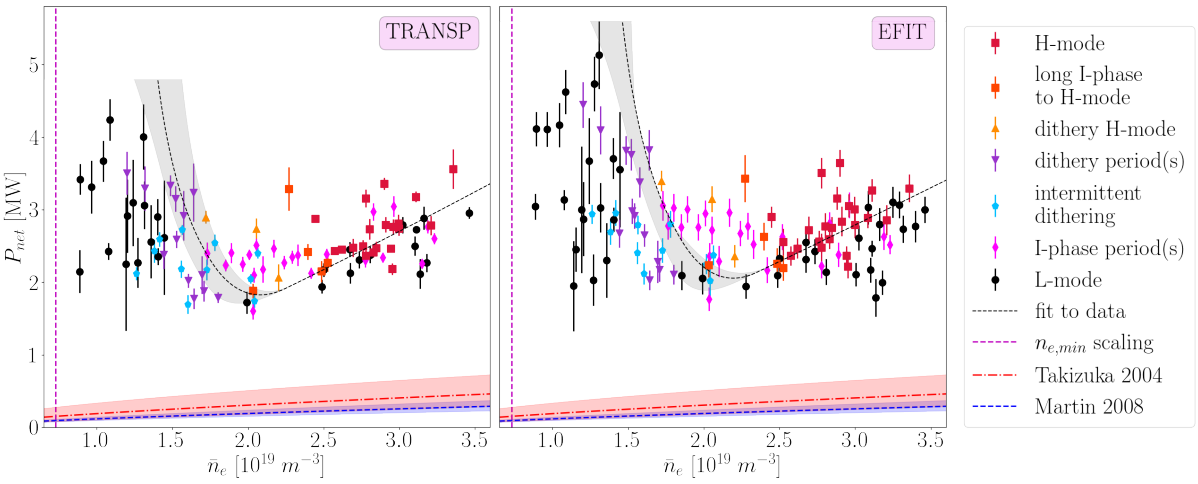

Figure 8: P_{net} with TRANSP (left) and EFIT (right) method, with the P_{LH} ITER scaling from Martin et al. and the low-aspect ratio modified version from Takizuka et al. The uncertainty range on the scalings include the uncertainty from the scaling law itself and the range in the included parameters for the shots studied here. The black dashed line in both plots is the fit performed for each data set. The magenta vertical line shows the projected $n_{e,min}$ from the scaling in Section 5.3.

with P_{LH}^{M} in MW, the line averaged density $\bar{n}_{e20}$ in 10^{20} m^{-3}, the magnetic field B_T in T and the plasma surface S in m^2. This scaling is not well suited to spherical tokamaks such as MAST and NSTX, though some attempts have been made to adjust it accordingly, for example Takizuka et al. [30]

$$P_{LH}^{T} = 0.072|B|_{out}^{0.7}\bar{n}_{e20}^{0.7}S^{0.9}\left(\frac{Z_{eff}}{2}\right)^{0.7}\frac{0.1A}{1-\left(\frac{2}{1+A}\right)^{0.5}} \tag{4}$$

where B_T has been replaced by the absolute B at the outer midplane of the plasma surface,

$$|B|_{out} = \left(\left(\frac{B_T \times A}{A+1}\right)^2 + \left(\frac{\mu_0 I_p}{2\pi a} \times (1+A^{-1})\right)^2\right)^{0.5}$$

taking into account the aspect ratio A, plasma current I_p and minor radius a, and correction factors for the effective charge Z_{eff} and aspect ratio, with a factor proportional to the fraction of untrapped particles, have been added. It should be noted that while MAST discharges were included in the Takizuka database, these were mainly ohmic H-modes with a ribbed divertor, and the installation of a new divertor with fan-shaped tiles [20] not long afterwards increased P_{LH} significantly. Another factor which increases P_{LH} is a higher toroidal plasma rotation [9], often present in beam-heated plasmas such as those in this data set, but not necessarily in purely ohmically-heated plasmas or plasmas with different heating methods. Figure 9 shows the MAST H-modes used in the Takizuka scaling plotted in green. Aside from the significant difference in the divertor between the two datasets, which is likely to play a prominent role in the different P_{LH} behaviour, for the new data set carbon coverage of the plasma facing components was increased, B_T, I_p and the major and minor radii were increased, elongation was decreased and triangularity increased.

Both scaling laws were compared with the data, and as can be seen in Figure 8, the observed P_{LH} is at least an order of magnitude higher than that predicted by either scaling law.

5.2 Fit to data

The data in the high density branch was fit with two free parameters, as $P_{LH} = \alpha \times \bar{n}_{e20}^{\gamma}$, with α containing all other dependencies aside from the density, which were kept consistent between discharges. The equations for the lines of best fit were

$$\text{TRANSP method: } P_{LH} = (11.35 \pm 2.30) \times \bar{n}_{e20}^{(1.19\pm0.16)} \tag{5}$$

$$\text{EFIT method: } P_{LH} = (10.41 \pm 2.20) \times \bar{n}_{e20}^{(1.09\pm0.17)} \tag{6}$$

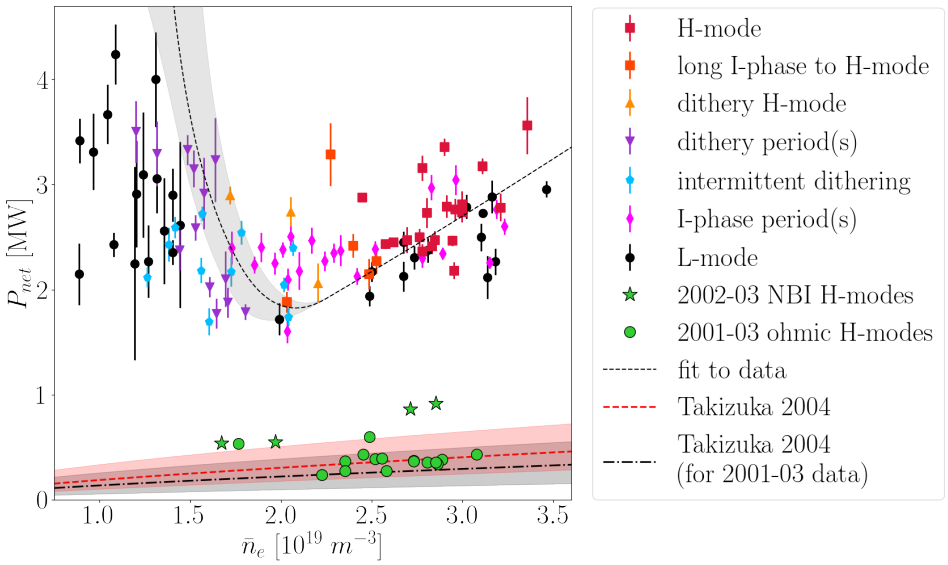

Figure 9: P_{net} vs $\bar{n}_e$ results of this study, compared with the ohmic and NBI-heated H-modes used in the Takizuka scaling [30] (in green). The Takizuka scaling (Equation 4) is plotted for the data from this study (red dashed line) and for the MAST data from 2001-2003 (black dot-dashed line).

for the results using P_{ohm} calculated by TRANSP and EFIT respectively. The density dependence thus has a 50-66% higher exponent than the scaling laws. The large discrepancy between the data and the scalings is mostly due to the leading factor (including other parameter dependencies). From the dataset analysed in this work, it is impossible to pinpoint where the discrepancy comes from, therefore further studies of other parameters and their effects on P_{LH}, as well as comparison with other spherical tokamaks are needed to illuminate the issue further. As STs usually operate in double null configuration, and the conventional tokamak database for scaling laws is based on single null geometries, the difference in P_{LH} could also be due to the configuration, rather than STs themselves.

For the different design concepts for STEP, the predicted P_{LH} can be compared to the available auxiliary heating power. If the Takizuka scaling is used for this, the ratio of P_{LH}/P_{aux} is found to be between 0.5 and 1.1 for leading STEP concepts, so H-mode operation appears feasible. As it is unclear which parameters are responsible for the large discrepancy between MAST data and the Takizuka scaling, the scaling law cannot yet be adjusted, and it is not currently possible to say whether the same increase in P_{LH} will be true for STEP as well. However, if one assumes that the leading factor and density dependence in Equation 4 can be modified to fit the MAST data, while the other parameter dependencies remain, the predicted P_{LH} is now 4-10 times higher than the available auxiliary heating power, making H-mode operation effectively impossible. This is likely to be an overestimate, as STEP will be heated with ECRH, which does not introduce the additional co-current plasma rotation that neutral beams do, and the significantly different divertor design is also likely to modify the P_{LH} behaviour. The limited understanding of how divertors and configurations affect P_{LH} especially for STs clearly demonstrates the need for more studies in this field.

5.3 Scaling for $n_{e,min}$

A scaling for the density at minimum P_{LH}, $n_{e,min}$, was derived by Ryter et al. [16]

$$n_{e,\mathrm{min}}^{\mathrm{scal}} \simeq 0.7 I_p^{0.34} B_T^{0.62} a^{-0.95} (R/a)^{0.4}$$

in 10^{19} m^{-3}, using units of MA, T and m. This was derived by combining the Martin scaling (3) for P_{LH} with the L-mode confinement scaling from the 1997 ITER database [31],

$$\tau_{\mathrm{th}} = 0.023 I_p^{0.96} B_T^{0.03} \kappa^{0.64} R^{1.83} (R/a)^{0.06} \bar{n}_e^{0.40} M_{\mathrm{eff}}^{0.20} P^{-0.73}.$$

To test the validity of this expression for MAST, the value of $n_{e,min}$ was calculated with the parameters of this experiment, returning $n_{e,\mathrm{min}}^{\mathrm{scal}} = 0.73 \times 10^{19}$ m^{-3}. This result is $\sim 3\times$ lower than the $n_{e,\mathrm{min}}$

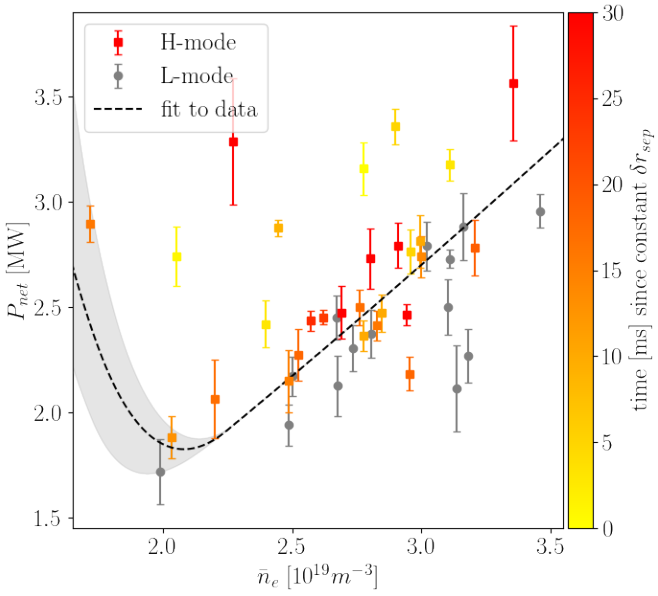

Figure 10: P_{net} vs $\bar{n}_e$ results for H-mode points (L-modes in grey), showing the time in ms between the beginning of the constant δr_{sep} region and the start of the H-mode period or the pre-H I-phase (if present). The colour bar has been restricted to 30 ms, though a number of points had values of 70-110 ms. Points towards the yellow end of the spectrum have very little delay between reaching the desired configuration and entering H-mode, so their $P_{net}(\bar{n}_e)$ combination must be interpreted as being $\geq P_{LH}$, not simply $= P_{LH}$.

observed, and actually a lower density than was studied in any of the shots in this experiment (see Figure 8). Based on the poor fit of the Martin P_{LH} scaling and the L-mode confinement scaling also originating from an ITER database the result is perhaps not surprising.

Modifying the Martin scaling to match the density dependence and leading factor of Equation 5, while keeping the B_T and S dependence the same, and assuming the same ratio of $\tau_E/\tau_{ei} = 9$ at minimum P_{LH}, we can derive an alternative scaling for $n_{e,min}$ using the MAST-modified P_{LH} scaling. The resulting scaling,

$$n_{e,\mathrm{min}}^{\mathrm{mod}} \simeq 5.15\ I_p^{0.51} B_T^{0.97} a^{-1.53} (R/a)^{0.54}$$

predicts $n_{e,min} = 5.5 \times 10^{19}$ m^{-3} for the parameters of this experiment, which is now $\sim 2.5\times$ higher than the observed $n_{e,min}$, and again outside of the studied density range.

5.4 Impact of H-mode control through δr_{sep}

Since the H-mode control technique described in Section 2, along with the limited ability to scan the heating power during a discharge, results in $P_{net}|_{t=t_{LH}} \geq P_{LH}$ rather than $= P_{LH}$, the P_{LH} curve must be drawn to approximately separate the regions of the plot that contain H-modes (i.e. are H-mode accessible) from those that do not. The H-mode points show much scatter. Colour-coding to represent how soon after the drop in δr_{sep} the transition occurred, makes the picture clearer. In Figure 10, the scale goes from yellow (L-H 0 ms after drop) to red (L-H $\geq$30 ms after drop). The points with P_{net} much larger than the minimum P_{net} found for H-modes in that density range generally show a shorter delay, and those with the longest delay appear to lie on or close to a potential P_{LH} curve.

5.5 Absorbed beam power calculations by TRANSP

The net power calculations were performed with the captured beam power returned by TRANSP as the auxiliary heating term, $P_{nbi} = P_{cap}$. When the terms in the energy balance equations for the heat flux were investigated, it became apparent that P_{cap} was larger than the sum of the beam heating powers absorbed by the electrons and ion, with a significant discrepancy especially for low-density plasmas. Further investigation revealed that P_{cap} only includes the shine-through losses, no further fast ion losses such as orbit or charge-exchange losses, and that these additional losses are significant for MAST plasmas,

especially for low densities. It is not clear why P_{cap} does not include these other losses, even though they are calculated by TRANSP, or why a more accurate absorbed power trace is not available. The following section includes a brief investigation into the sources of the beam losses in Section 6.3, and Section 6.4 describes the effect of using the beam power absorbed by the plasma $P_{heat,tot}$ instead of the captured beam power P_{cap} in the net power calculations, with results shown in Figure 16. The more comprehensive TRANSP analysis required for these calculations was performed on a limited set of H-mode and dithery transitions, so the full power threshold results of Figures 6 and 8 are not yet available for the adjusted P_{net}.

6 Ion and electron heat flux

L-H transition theory as described by Malkov et al. [18] connecting the microscopic transition dynamics and the macroscopic physics of the power threshold suggests that the increase in P_{LH} for decreasing $\bar{n}_e$ in the low-density branch is due to a decrease in both the collisional electron-to-ion energy transfer and the heating fraction coupled to ions. Both of these processes strengthen the edge electric field shear which is needed for the L-H transition. The increase in P_{LH} along the high-density branch in turn is suggested to be caused by an increase of the damping of turbulence-driven shear flows due to increasing ion collisionality.

Experimental studies on ASDEX-Upgrade [16] and C-Mod [17] have postulated that the E_r well is driven mainly by the ion heat flux at the plasma edge, $q_{i,edge}$, through its role in the increase of the ion pressure gradient $|\nabla p_i|$. For heating methods of electron cyclotron resonant heating (ECRH) on AUG and ion cyclotron heating (ICH) on C-Mod, the surface integrated edge ion heat flux $Q_{i,edge}$ was found to increase linearly with $\bar{n}_e$, even in the low-density branch where P_{LH} has a non-monotonic density dependence. These results suggested a possibly critical $Q_{i,edge}$ per particle for H-mode access. The electron heat flux $Q_{e,edge}$ on AUG followed a similar $\bar{n}_e$ dependence to P_{LH}. It was suggested that a reduced electron-ion coupling at low density could therefore contribute to a higher P_{LH} requirement [16]. Studies on AUG using NBI heating showed no density dependence for either $Q_{i,edge}$ or $Q_{e,edge}$, and in cases of no additional ECRH heating (NBI only) $Q_{e,edge} \sim Q_{i,edge}$.

6.1 Determining Q_i and Q_e for MAST

To compare the previous results with data from MAST, profiles of the ion and electron heat flux Q_i and Q_e are produced using the interpretative transport code TRANSP. Profiles of electron density n_e, temperature T_e and ion temperature T_i are provided by Thomson scattering (TS) and charge exchange (CXRS) diagnostics and fitted before being utilised by TRANSP while solving the energy balance equations

$$\frac{3}{2}\frac{\partial}{\partial t}\left(n_i k_B T_i\right) + \nabla \cdot q_i + \nabla \cdot \left(\frac{5}{2} n_i k_B T_i v_i\right) - v_i \cdot \nabla \left(n_i k_B T_i\right) = p_{heat} + p_{neut} + q_{ie} - p_{cx} \tag{7}$$

$$\frac{3}{2}\frac{\partial}{\partial t}\left(n_e k_B T_e\right) + \nabla \cdot q_e + \nabla \cdot \left(\frac{5}{2} n_e k_B T_e v_e\right) - v_i \cdot \nabla \left(n_i k_B T_i\right) = p_{ohmic} + p_{heat} - p_{ioniz.} - p_{rad} - q_{ie} \tag{8}$$

where n_i is the ion density, v_e and v_i are the electron and ion velocities, respectively, and q_e and q_e are the electron and ion conductive heat flux. All terms are power densities, in units of MWm^{-3}. Along with the conductive heat transport, the left hand sides contain the rate of energy change (gain) and the convective heat transport, while the right hand sides contain the source and sink terms. The largest source terms are generally the auxiliary and ohmic heating terms, p_{heat} and p_{ohmic}, while the radiated power p_{rad} and the ion-electron coupling q_{ie} can be significant too. The ions further gain energy from the ionisation of neutral particles by electrons p_{neut} and lose energy through charge exchange collisions p_{cx}, while the energy lost by electrons through ionising collisions with neutrals is given by $p_{ioniz.}$. The terms are integrated and the results in units of MW can be compared with P_{net}. Both TS and CXRS have variable data quality, and the profile fitting introduces uncertainties to the calculated values of the heat flux components. The T_i data from CXRS has been treated with a de-smearing correction to improve its accuracy. Since T_i data is not always available in the SOL and edge regions, the T_i profiles had to be extrapolated. This introduces further uncertainties, though their magnitudes have not been determined.

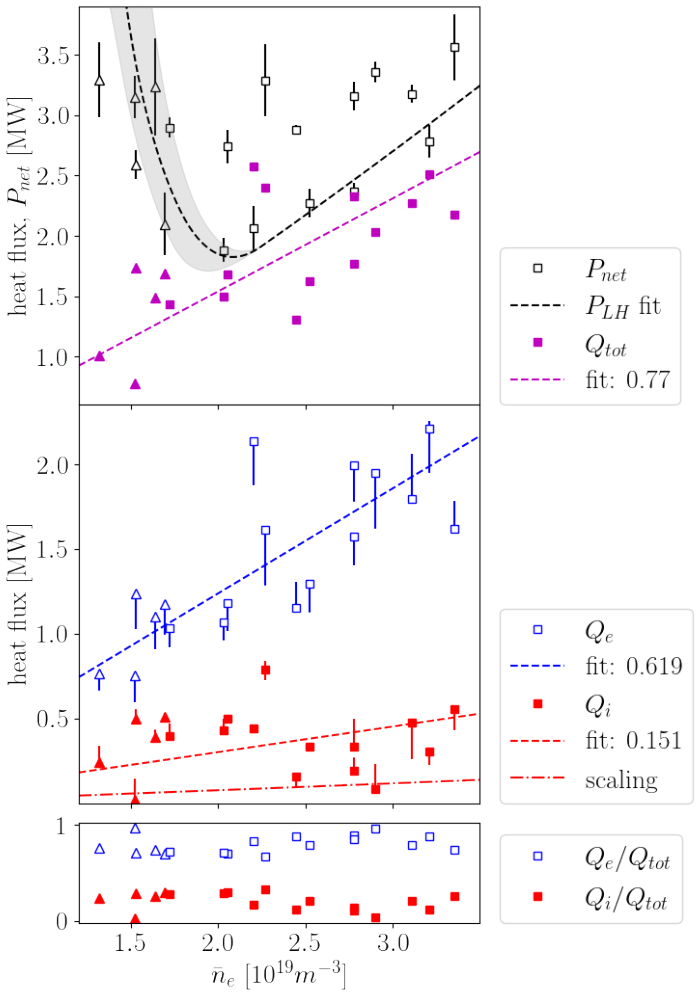

Figure 11: Top: P_{net} and total heat flux Q_{tot} values shown for selected L-H transitions (squares) and some low-density dithery periods (triangles). Also shown are the P_{LH} density fit from Section 5 and a linear density fit for Q_{tot}. Middle: The Q_e and Q_i values at the separatrix for these points, with corresponding linear density fits and the Q_i density scaling from [17]. The error bars represent the range of values between $0.85 < \rho_N < 1.0$. Bottom: The distribution of total heat flux in Q_e and Q_i, showing no clear systematic variation in density.

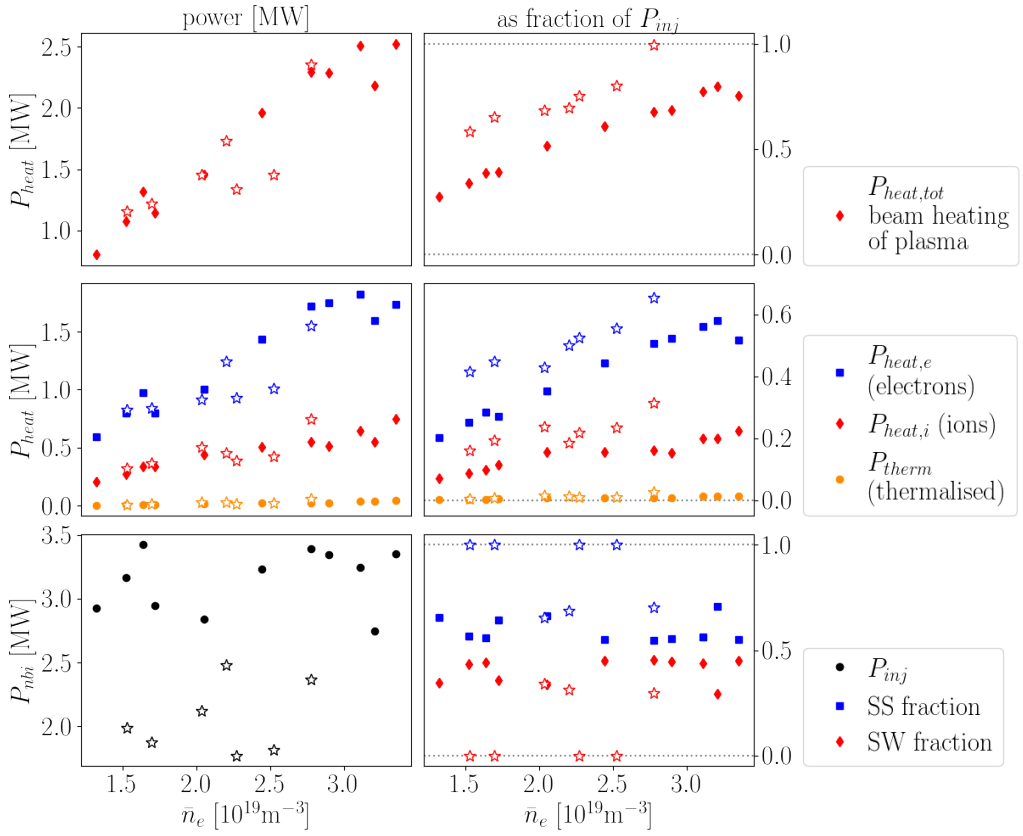

Figure 12: For all considered H-mode and dithery shots, the total beam heating of the plasma (top) and its components (heating of electrons, heating of ions and thermalised beam ions) (middle). The right hand side plots show the values normalised to the injected beam power. The bottom two plots show the injected beam power P_{inj} (left) and the proportions of P_{inj} in the two beams, South and Southwest. In all plots, the open star symbols mark a set of transitions which occurred at lower P_{inj} (< 2.7MW) and had lower levels of fast ion losses.

6.2 Heat flux results from MAST

Figure 11 shows the results of the heat flux analysis at the separatrix against line-averaged electron density for selected L-H transitions (squares) and additional dithery periods in the low density region (triangles). The associated P_{net} values are shown alongside the total heat flux $Q_{tot} = Q_e + Q_i$ in the top plot. The non-monotonic density dependence of P_{LH} is contrasted with the fairly linear density dependence of Q_{tot}, such that a low-density shot has a lower Q_{tot} than a high-density shot with the same P_{net}. The middle plot shows the electron and ion heat fluxes, Q_e and Q_i respectively. Since occasional mismatches between diagnostic data and EFIT equilibrium introduce a small uncertainty in the separatrix location, error bars are plotted on Q_e and Q_i showing the range of values for $0.85 < \rho_N < 1.0$ with ρ_N as defined by TRANSP. Previous studies found a linear $\bar{n}_e$ dependence for Q_i, so the data was fit with linear fits for both Q_i and Q_e, with $Q_{i,fit} = 0.151\bar{n}_e$ and $Q_{e,fit} = 0.619\bar{n}_e$ for units of MW and $10^{19}m^{-3}$. The scaling for Q_i from AUG and C-Mod [17],

$$Q_{i,fit}^{LH} = 0.0029\bar{n}_e^{1.05\pm0.1} B_T^{0.68\pm0.3} S^{0.93\pm0.2}$$

predicts $Q_{i,scaling} \simeq 0.037\bar{n}_e$ for MAST (shown as a dot-dashed line), which is lower than that found for the data here. However, the Q_i data shows significant scatter and the linear fit is not obviously recognisable. The Q_i values mostly lie above the scaling from [17]. The linear density dependence of Q_e was not seen on other devices. As can be seen in the bottom plot, the fraction of Q_{tot} from either Q_e or Q_i appear to remain fairly constant throughout the density range, with Q_i usually contributing $\sim 12 - 30\%$.

The terms in the energy balance are investigated to identify the sources of the density dependence. The largest contributions to Q_e and Q_i are the heating terms, specifically the heating by beams. These are also the terms which show the clearest density dependence, with $P_{heat,e} \approx 0.53\bar{n}_e$ and $P_{heat,i} \approx$

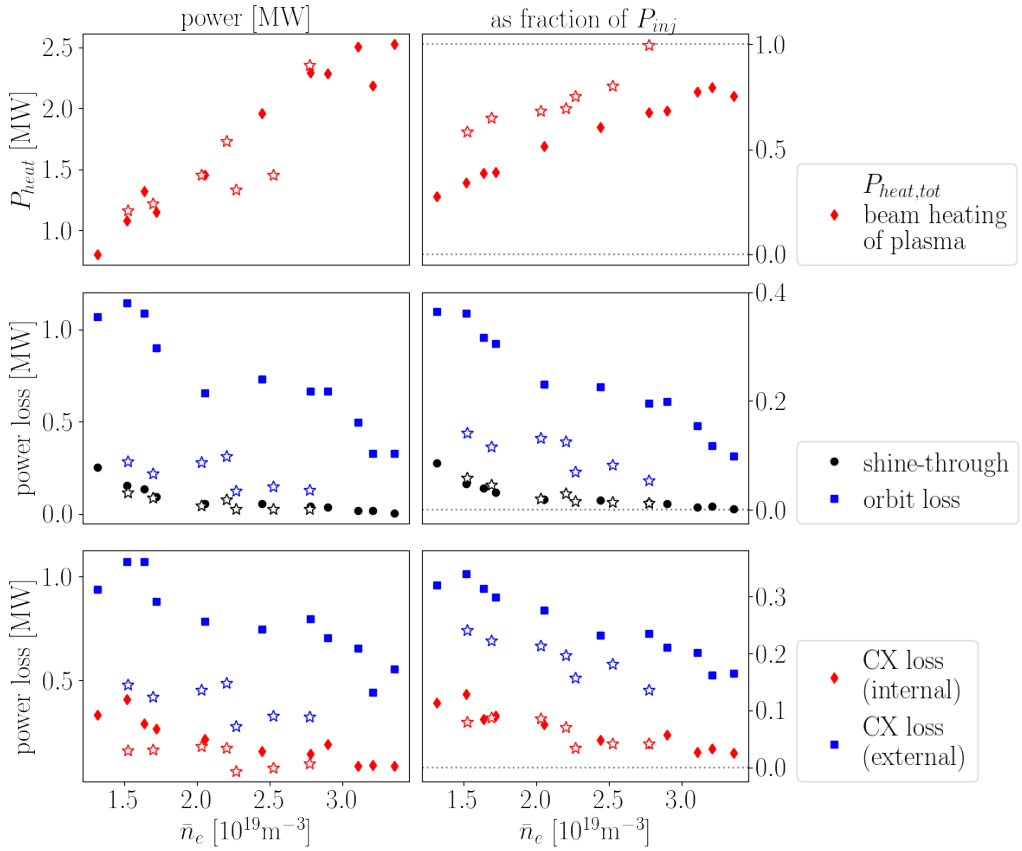

Figure 13: The total beam heating of the plasma (top), shine-through and orbit losses (middle), and charge-exchange (re-neutralisation) losses inside and outside of the LCFS (bottom). The right hand side shows the same quantities normalised to P_{inj}. The open star symbols mark a set of transitions which occurred at lower P_{inj} (< 2.7MW) and had lower levels of fast ion losses.

$0.2\bar{n}_e$. The total beam heating of the plasma is $P_{heat,tot} = P_{heat,e} + P_{heat,i} + P_{therm}$, where the power from thermalised beam ions P_{therm} also has a linear density dependence but an insignificant magnitude compared with the heating of electrons and ions. Since $P_{heat,tot}$ was found to be much lower than the captured beam power P_{cap}, the beam heating and loss terms were studied in more detail to identify the cause of the discrepancy. As Figure 12 shows, there is a general trend of lower beam heating of the plasma $P_{heat,tot}$ for lower densities, independent of injected beam power P_{inj}. If $P_{heat,tot}$ is normalised to P_{inj}, we can see that in addition to the decreasing fraction of injected beam power heating the plasma (from $\sim 80\%$ at high $\bar{n}_e$ to $\sim 30\%$ at low $\bar{n}_e$), there is a second set of transitions which have higher heating fractions than transitions at equivalent density. These are marked with open star symbols in Figures 12 and 13. In the bottom left plot of Figure 12, it can be seen that these points all had lower values of P_{inj}. These results suggest that the fraction of injected beam power which contributes to heating the plasma decreases for lower densities as well as for higher injected powers.

6.3 Reduced heating efficiency at low density

The clear density dependence of the beam heating of the plasma $P_{heat,tot}$, with low-density plasmas of the same injected NBI power P_{inj} showing much lower heating than equivalent high-density plasmas, suggests a reduced efficiency of NBI and associated higher fast ion losses for lower densities. Figure 13 shows the losses which have been identified as possessing a density dependence with higher losses at low density. These are shine-through losses, orbit losses (beam ion is lost from confinement on its first poloidal orbit), and charge-exchange (re-neutralisation of beam ions) losses both inside and outside of the separatrix. Shine-through losses are taken into account in the P_{net} study with the usage of P_{cap}, but while they show a clear density dependence, their magnitude is much too low to account for the trend in $P_{heat,tot}$. The largest loss terms are orbit losses and charge-exchange losses outside of the LCFS. As previously, the open star symbols denote a set of data with lower P_{inj}, and both orbit losses and charge-

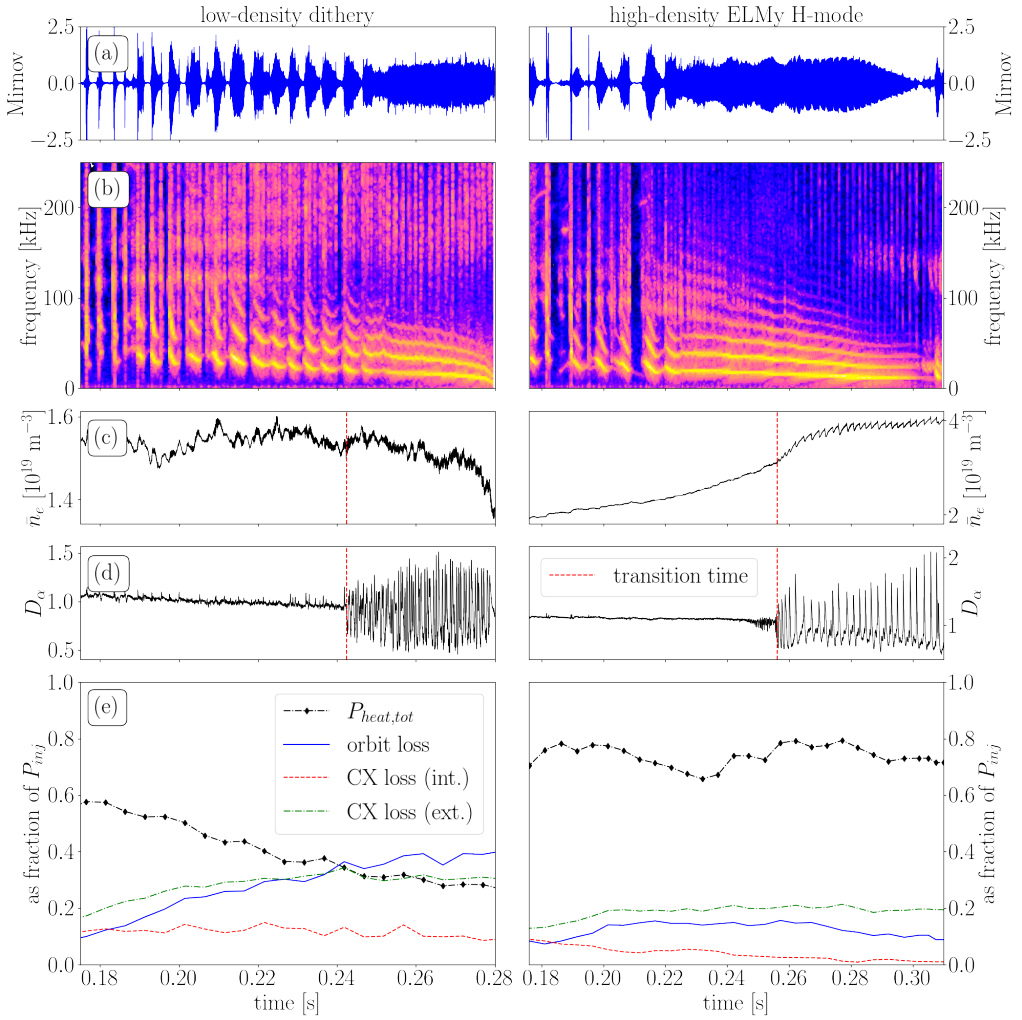

Figure 14: Representative examples of a low-density shot (27771, left) with a transition to a dithery period at $t = 0.242$s and $\bar{n}_e = 1.52 \times 10^{19}$ m^{-3}, and a high-density shot (27036, right) with a transition to an ELMy H-mode at $t = 0.256$s and $\bar{n}_e = 3.11 \times 10^{19}$ m^{-3}. The plots show: the signal (a) and spectrogram (b) of a Mirnov coil, the line-averaged density (c) and D_α (d) traces, as well as (e) the beam heating of the plasma and selected loss terms as calculated by TRANSP, normalised to P_{inj}.

exchange losses outside of the LCFS are significantly lower for this set. This discrepancy is retained even with a normalisation to P_{inj}. Fast ion losses beyond those from classical collisions are estimated with TRANSP by setting an ad hoc beam-ion diffusion coefficient, anomalous fast ion diffusivity $D_{an.}$, which is added to the classical diffusion model to approximate the effect of fast ion redistribution and losses observed in experiments [32]. As the majority of the neutron emission on MAST comes from beam-thermal and beam-beam ion reactions [33, 34], the level of fast ion diffusivity can be estimated by attempting to match the TRANSP-predicted neutron rate to the measured neutron rate. The existence of the MHD modes responsible for fast ion losses must then be verified separately.

To investigate whether the increased fast ion losses at low densities or high beam powers estimated by TRANSP can be observed experimentally, the MHD activity was studied with Mirnov coil signals. Figure 14 shows representative examples of a low-density shot with a transition to a dithery period and a high-density shot with a transition to an ELMy H-mode. The low-density shot has a smaller fraction of the injected beam power heating the plasma (0.34 vs 0.77 at transition time) with corresponding higher levels of power losses and a higher anomalous diffusion value (3.5 m^{2}s^{-1} vs 2.5 m^{2}s^{-1}). The signal and spectrogram of a Mirnov coil are plotted alongside the line-averaged density and upper D_α traces for the entire I_p flat top. The bottom plots show the beam heating of the plasma $P_{heat,tot}$, as well as orbit and charge-exchange losses as calculated by TRANSP. The discharges in this study generally start out with chirping modes, possibly fishbones or TAEs, which then develop into a long-lived mode (LLM) of

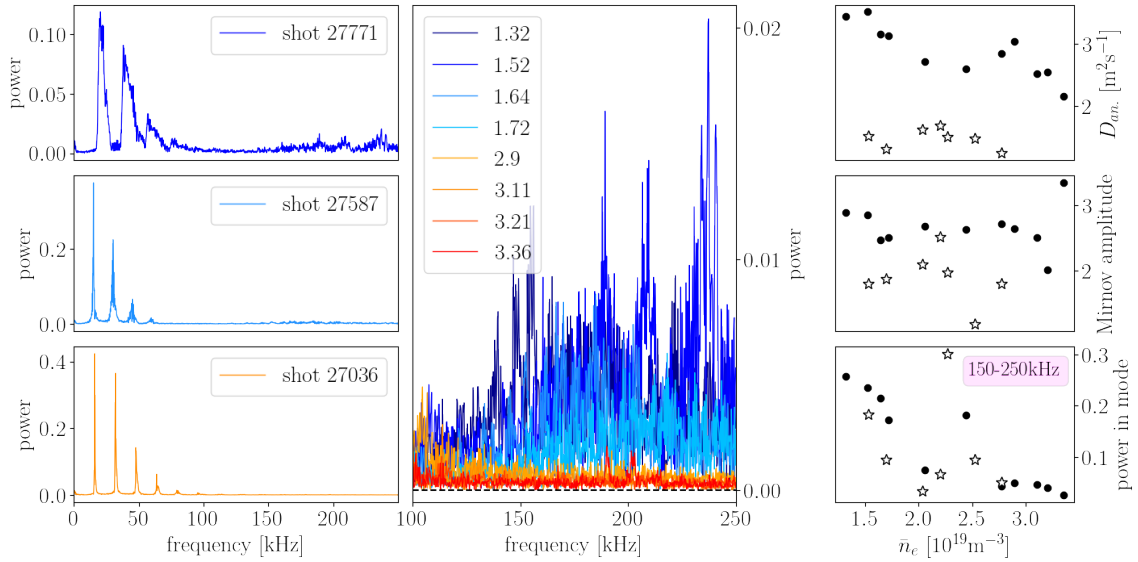

Figure 15: Mirnov signal spectra during the transition time of a selection of low- and high-density shots. The left hand side shows two low-density shots (27771 and 27587) and a high-density shot (27036). The relevant frequency range is shown in the middle for four low-density and four high-density shots (legend labels show density in 10^{19} m^{-3}), showing the higher activity for lower densities. The right hand side shows the anomalous fast ion diffusivity $D_{an.}$ in the TRANSP runs, the amplitude of the Mirnov signal and the power in the 150-250kHz frequencies of the Mirnov signal. The open star symbols mark a set of transitions which occurred at lower P_{inj} (< 2.7MW) and had lower levels of fast ion losses.

15-20kHz, an internal kink mode matching the plasma rotation frequency [35], visible in the spectrogram with harmonics. Comparing the two cases in Figure 14, the low-density discharge has a longer period of chirping modes, and strong broadband mode activity in the frequencies 150-250kHz, which is largely absent from the high-density case. The increased activity in the 150-250kHz frequency range is found in all low-density shots. A similar picture is found when comparing shots of similar density but different injected beam powers, with the low-P_{inj} shots showing reduced activity in this frequency range.

Figure 15 shows spectra of the Mirnov signal for $t_{LH} \pm 2$ms. The high-density shot of Figure 14 (27036, bottom left) is entirely dominated by the LLM, while the low-density shot (27771, top left) transitions during the chirping mode phase, so the low-frequency peaks are much broader, and the increased broadband activity at frequencies above 150kHz are clearly visible. An example of a low-density shot with a transition during the long-lived mode is shown in the middle left plot. The increased activity at higher frequencies is harder to see here, so four low-density and four high-density shots are shown on the middle plot for frequency range 100-250kHz. The low-density shots all clearly have increased power in the higher frequencies, with a density dependence visible for both low- and high-density shots.

The right hand side of Figure 15 shows the anomalous fast ion diffusivity values $D_{an.}$ used in the TRANSP runs, the amplitude of the signal in a Mirnov coil, and the power contained in the Mirnov signal in the frequency range of $150 - 250$kHz. The anomalous diffusion rate is larger for lower densities as well as for higher injected powers, suggesting that TRANSP assumes higher fast ion redistributions or losses for those situations. Some evidence of this can be seen in the Mirnov signals, with the power contained in the broadband MHD activity of frequency range $150 - 250$kHz showing a strong density dependence. The Mirnov signal amplitude shows no clear density dependence but appears to be lower for low P_{inj}, supporting the assumed lower fast ion losses for these discharges.

A number of previous studies into fast ion physics on MAST [32, 33, 34, 36] have shown that stronger activity of certain MHD modes, notably frequency-chirping fishbones, toroidal Alfven eigenmodes (TAEs), as well as LLMs [37], leads to increased redistribution and loss of the fast ion population. As was found in this paper, previous studies have shown that these modes are excited at higher rates and amplitudes in low-density plasmas and in discharges with higher injected beam powers [33, 36]. Depending on the density and NBI power, earlier studies on MAST have found that $D_{an.} \sim 0 - 3$ m^{2}s^{-1} were required to match neutron rates, which mostly agrees with the findings here.

6.4 Consequences for P_{LH} curve

These results appear to suggest that neutral beam heating becomes much less efficient with lower plasma densities, and also separately with higher injected beam power. While the lower heating efficiencies for low densities was also found on ASDEX Upgrade and other devices, the suggested explanation of reduced electron-ion coupling does not appear to be a major concern here, instead the diminished heating efficiency affects both ion and electron heating and is likely to be caused by fast ion losses degrading beam performance. An alternative version of the $P_{net}(\bar{n}_e)$ plot can be created by including the beam heating of the plasma $P_{heat,tot}$ as the P_{nbi} term instead of the captured beam power P_{cap}. The results are shown in Figure 16. Aside from one outlier, a H-mode transition after a sawtooth event, the scatter in the H-mode points has been significantly reduced. A fit to the H-mode points returns $P_{LH} = 11.27 \times \bar{n}_e^{1.33}$, which has a higher density exponent than the previous fit and widely used scalings. While the low-density branch is not as clearly visible in the new H-mode points, the dithery points all lie above the fit, suggesting that a low-density branch or low-density limit still exists and is not entirely explained by the reduced beam heating efficiency. The reduced scatter can be traced back to the strong density dependence of $P_{heat,tot}$, shown in the top right of Figure 16, while the higher P_{net} values for the dithery transitions are due to lower values of dW/dt, as seen in the bottom right plot. dW/dt appears to follow an inverse U-curve, although the maximum occurs at a higher density than $n_{e,min}$. In a practical use of P_{LH} scalings, the higher injected NBI power required for H-mode access at low densities is also still relevant. For AUG, in the ECRH heated case the linear $\bar{n}_e$ dependence of Q_i was compensated by Q_e following a similar $\bar{n}_e$ dependence as P_{LH} (which is not the case on MAST), while in the NBI heated case Q_{tot} was apparently constant throughout the low-density branch. This mismatch in the $\bar{n}_e$ dependence of Q_{tot} and P_{LH} is possibly equivalent to the MAST case where shots with the same P_{net} have different Q_{tot}, and could be an NBI feature.

7 Summary and Conclusion

Results from a power threshold analysis and electron and ion heat flux analysis of L-H transitions on MAST have been presented, which show the first evidence of the parameter space of the low-density branch on MAST. With this observation, the density dependence of P_{LH} shows a characteristic non-monotonic behaviour. This was made possible by studying the character of H-modes at different densities, with pre-H I-phases seen to grow longer at lower densities, and low-density H-modes appearing dithery. Intermediate states visible at the P_{LH} boundary across the density range were investigated and categorised mainly based on their D_α signals, with I-phases, identical to those preceding H-modes, present throughout at a characteristic oscillation frequency range of 3-4 kHz, and intermediate states in low-density plasmas containing dithery periods with irregular fluctuations at frequencies 1.5-2.5kHz. Dithery periods and I-phases are potentially both versions of limit-cycle-oscillations, but their D_α traces are distinct, in addition to the different frequencies mentioned they also vary in skewness, with the regular I-phase oscillations having skewness close to zero. The P_{net} vs $\bar{n}_e$ plot shows the presence of a high-density and a low-density branch, with $n_{e,min} \simeq (2.3 \pm 0.2) \times 10^{19} m^{-3}$ with a minimum P_{LH} of around 2MW. The boundary of the low-density branch contains a broad region of dithery periods. Inclusion of P_{rad} in the P_{net} calculations did not change the qualitative picture. Comparisons with the Martin scaling [19] and the Takizuka scaling [30] showed that they under-predict P_{LH} by at least an order of magnitude, while a scaling for $n_{e,min}$ by Ryter [16] is 3× lower than the observed value. A fit to the high-density branch of the data returned $P_{LH} = (11.35 \pm 2.30) \times \bar{n}_{e20}^{(1.19 \pm 0.16)}$. The cause of the discrepancy between MAST data and scalings is likely to lie in parameters which could not be investigated at this time, and more studies are required to pinpoint the cause of higher P_{LH} for spherical tokamaks. Previous work suggested that there is a critical ion heat flux in the edge for H-mode access, and that the low-density branch could be explained by a reduced electron-ion coupling at lower density. To investigate this on MAST, the edge ion Q_i and electron heat fluxes Q_e for this data set were calculated using TRANSP. Q_e showed a linear $\bar{n}_e$ dependence into the low-density branch, while Q_i showed no clear $\bar{n}_e$ dependence. The total heat flux Q_{tot} has a linear $\bar{n}_e$ dependence independent of P_{net}. This was investigated further, and the beam heating of electrons and ions was found to have a strong linear $\bar{n}_e$ dependence. The total beam heating of the plasma $P_{heat,tot}$ ranges from 80% of the injected beam power P_{inj} at high densities to 30% at low densities. The required higher P_{inj} for low-density transitions appears to be mostly related to the reduced beam heating efficiency and affects both ions and electrons. Both a lower plasma density and a higher P_{inj} was predicted by TRANSP to have higher fast ion losses, mostly orbit losses and charge-exchange losses. The captured beam power P_{cap} calculated by TRANSP

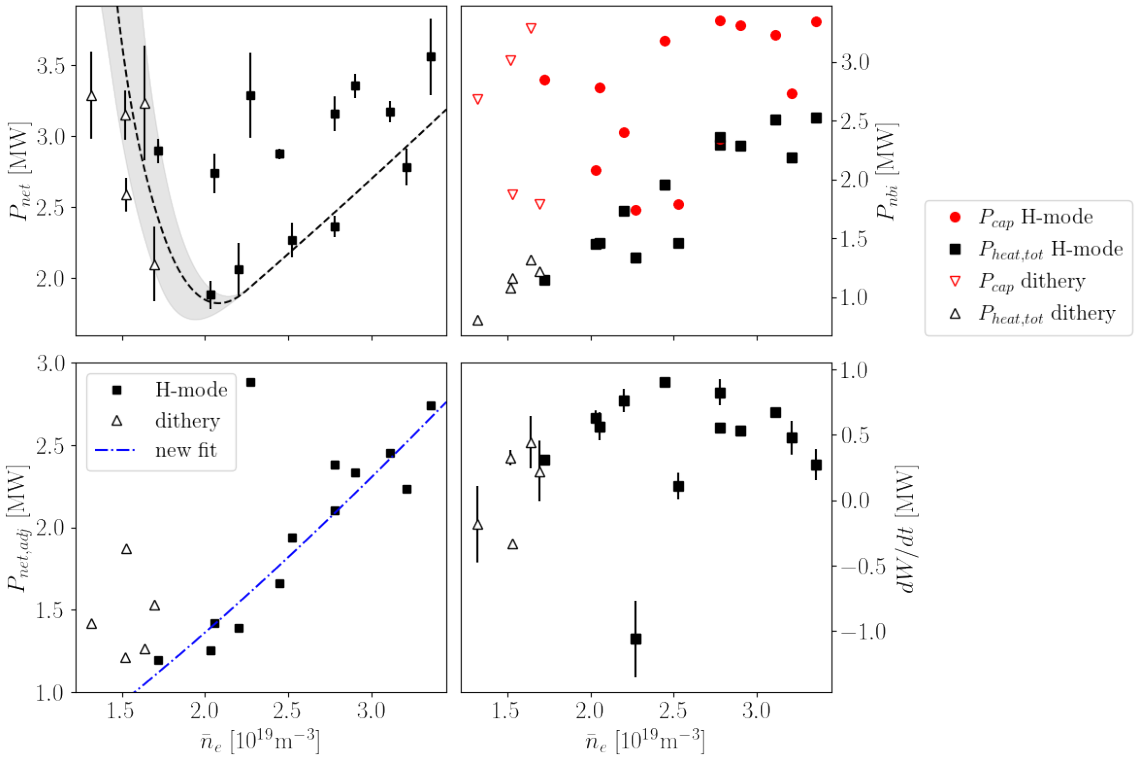

Figure 16: P_{net} vs $\bar{n}_e$ for the previous method (top left), which uses $P_{nbi} = P_{cap}$, and a new version of P_{net} (bottom left), which uses the calculated beam heating of electrons and ions, $P_{nbi} = P_{heat,tot}$, instead. The values are significantly lower, with reduced scatter in the H-mode points. A fit to the H-mode points is shown in blue, and the dithery points all lie above it, suggesting that a low-density branch or limit might still exist. P_{cap} and $P_{heat,tot}$ are compared in the top right plot, with the reduced scatter in $P_{heat,tot}$ visible. The higher P_{net} values for the dithery transitions in the adjusted method are due to the lower values of dW/dt, visible in the bottom right. dW/dt appears to follow an inverse U-curve, although the maximum occurs at a higher density than $n_{e,min}$. The outlier H-mode point at $dW/dt = -1.1$ MW occurs after a large sawtooth event.

only includes the shine-through losses, not the orbit and charge-exchange losses, so significantly overestimates the absorbed beam power for MAST. The higher values of anomalous diffusion $D_{an.}$ for low densities and higher P_{inj} can be justified by inspection of Mirnov signals, which show stronger chirping modes and a higher broadband MHD activity in the $150-250$kHz range. The power in $f \sim 150-250$kHz appears to have an inverse density dependence, and the Mirnov signal amplitude shows a P_{inj} dependence, consistent with higher fast ion losses for low densities and higher P_{inj}. These results agree with previous studies on fast ion physics on MAST. If the net power calculation is adjusted to include all fast ion losses, not just shine-through losses, with $P_{nbi} = P_{heat,tot}$ instead of P_{cap}, the scatter in the H-mode points largely disappears, and a new density fit of $P_{LH} = 11.27 \times \bar{n}_e^{1.33}$ can be found. While the steep gradient of the low-density branch is reduced in this case, the low-density dithery periods lie above the P_{LH} fit and some kind of low-density branch or limit likely still exists.

Acknowledgements

Many thanks to B. Patel, S. Henderson, H.-T. Kim and D. Keeling for helpful discussions, and to C. Wade and L. Kogan for providing additional data. This work was supported by the Engineering and Physical Sciences Research Council grants [EP/L01663X/1] and [EP/W006839/1].

References

[1] F. Wagner, *et al.*, *Physical Review Letters* **49**, 5 (1982).

[2] ITER Organisation, *ITER research plan within staged approach, ITR-Report 18-003* (2018).

[3] C. F. Maggi, *et al.*, *Nuclear Fusion* **54**, 023007 (2014).

[4] Y. Andrew, *et al.*, *Plasma Physics and Controlled Fusion* **48**, 479 (2006).

[5] Y. Ma, *et al.*, *Nuclear Fusion* **52**, 17 (2012).

[6] Y. Ma, J. W. Hughes, A. E. Hubbard, B. LaBombard, J. L. Terry, *Plasma Physics and Controlled Fusion* **54**, 6 (2012).

[7] Y. Andrew, *et al.*, *Plasma Physics and Controlled Fusion* **46**, 7 (2004).

[8] T. Fukuda, *et al.*, *Nuclear Fusion* **37**, 15 (1997).

[9] P. Gohil, G. McKee, D. Schlossberg, L. Schmitz, G. Wang, *Journal of Physics: Conference Series* (IOP Publishing, 2008), vol. 123, p. 012017.

[10] G. McKee, *et al.*, *Nuclear Fusion* **49**, 115016 (2009).

[11] F. Ryter, *et al.*, *Nuclear Fusion* **53**, 113003 (2013).

[12] W. L. Zhong, *et al.*, *Nuclear Fusion* **60**, 7 (2020).

[13] I. Cziegler, A. E. Hubbard, J. W. Hughes, J. L. Terry, G. R. Tynan, *Physical Review Letters* **118**, 5 (2017).

[14] K. Ida, *et al.*, *Physical Review Letters* **65**, 4 (1990).

[15] R. M. McDermott, *et al.*, *Physics of Plasmas* **16**, 12 (2009).

[16] F. Ryter, *et al.*, *Nuclear Fusion* **54** (2014).

[17] M. Schmidtmayr, *et al.*, *Nuclear Fusion* **58**, 9 (2018).

[18] M. A. Malkov, P. H. Diamond, K. Miki, J. E. Rice, G. R. Tynan, *Physics of Plasmas* **22**, 12 (2015).

[19] Y. R. Martin, T. Takizuka, *Journal of Physics: Conference Series* **123**, 11 (2008).

[20] A. Darke, R. Hayward, G. Counsell, K. Hawkins, *Fusion Engineering and Design* **75-79**, 285 (2005). Proceedings of the 23rd Symposium of Fusion Technology.

[21] M. Greenwald, *Plasma Physics and Controlled Fusion* **44**, R27 (2002).

[22] H. Meyer, *et al.*, *Plasma Physics and Controlled Fusion* **50**, 9 (2008).

[23] F. Ryter, *et al.*, *Nuclear Fusion* **36**, 48 (1996).

[24] L. L. Lao, H. S. John, R. D. Stambaugh, A. G. Kellman, W. Pfeiffer, *Nuclear Fusion* **25**, 12 (1985).

[25] R. Hawryluk, *in Physics of Plasma Close to Thermonuclear Conditions (Proc. Course Varenna, 1979), CEC, Brussels* (1980), vol. 1.

[26] D. A. Homfray, *et al.*, *23rd IEEE/NPSS Symposium on Fusion Engineering* (2009), pp. 1–4.

[27] P. B. Snyder, *et al.*, *Physics of Plasmas* **9**, 7 (2002).

[28] A. Kirk, *et al.*, *Plasma Physics and Controlled Fusion* **46**, 551 (2004).

[29] G. Birkenmeier, *et al.*, *Nuclear Fusion* **56** (2016).

[30] T. Takizuka, *Plasma Physics and Controlled Fusion* **46**, A227 (2004).

[31] S. Kaye, *et al.*, *Nuclear Fusion* **37**, 1303 (1997).

[32] M. Turnyanskiy, *et al.*, *Nuclear Fusion* **53**, 053016 (2013).

[33] D. Keeling, *et al.*, *Nuclear Fusion* **55**, 013021 (2014).

[34] O. Jones, *et al.*, *Plasma Physics and Controlled Fusion* **57**, 125009 (2015).

[35] I. T. Chapman, *et al.*, *Nuclear Fusion* **50**, 16 (2010).

[36] I. Klimek, *et al.*, *Nuclear Fusion* **55**, 023003 (2015).

[37] M. Cecconello, *et al.*, *Plasma Physics and Controlled Fusion* **57**, 014006 (2014).